




Properties and observables of massive galaxies in self-interacting dark matter cosmologies

Claudio Mastromarino,^{1,2★} Giulia Despali^{1,2,3,4} , Lauro Moscardini^{1,2,4,5} , Andrew Robertson^{1,6} ,
Massimo Meneghetti^{4,5} and Matteo Maturi³

¹*INFN-Sezione di Roma ‘Tor Vergata’, Via della Ricerca Scientifica, 1, 00133, Roma, Italy*

²*Dipartimento di Fisica e Astronomia ‘A. Righi’, Alma Mater Studiorum Università di Bologna, Via Piero Gobetti 93/2, I-40129 Bologna, Italy*

³*Institut für Theoretische Astrophysik, Zentrum für Astronomie, Heidelberg Universität, Albert-Ueberle-Straße 2, 69120, Heidelberg, Germany*

⁴*INAF-Osservatorio di Astrofisica e Scienza dello Spazio di Bologna, Via Piero Gobetti 93/3, I-40129 Bologna, Italy*

⁵*INFN-Sezione di Bologna, Viale Bertini Pichat 6/2, I-40127 Bologna, Italy*

⁶*Jet Propulsion Laboratory, California Institute of Technology, 4800 Oak Grove Drive, Pasadena, CA 91109, USA*

Accepted 2023 June 18. Received 2023 June 12; in original form 2022 November 28

ABSTRACT

We use hydrodynamic cosmological simulations to test the differences between cold and self-interacting dark matter models (CDM and SIDM) in the mass range of massive galaxies ($10^{12} < M_{200}/M_{\odot} h^{-1} < 10^{13.5}$). We consider two SIDM models: one with constant cross-section $\sigma/m_{\chi} = 1 \text{ cm}^2 \text{ g}^{-1}$ and one where the cross-section is velocity-dependent. Despite a weak trend in mass, we find that with the inclusion of baryons the differences between SIDM and CDM density profiles observed in the dark-matter-only case are almost erased. We also search for signatures of SIDM in the distribution of strong lensing Einstein radii and find that the distributions derived from CDM and SIDM hydro runs are both comparable to observational samples of strong lenses. We find that, looking at the total matter distribution, the interplay between self-interactions and baryons can greatly reduce the expected differences between CDM and SIDM models at this mass scale, making the discrimination between these DM models challenging. However, looking at the dark matter/baryonic fractions in the inner region of the haloes we show that the deviations of SIDM from CDM can still be found considering these components separately. These results highlight that one of the most promising paths to discriminate between CDM and SIDM is to focus on techniques able to distinguish between the dark matter and baryonic components in galaxies and clusters.

Key words: gravitational lensing: strong – methods: numerical – galaxies: elliptical and lenticular, cD – galaxies: haloes – X-rays: galaxies – dark matter.

1 INTRODUCTION

The dominant hypothesis for the formation and evolution of cosmic structure in our Universe is the Λ cold dark matter (Λ CDM) model, in which dark matter (DM) particles are non-relativistic and collisionless. This standard model is able to explain several fundamental properties of galaxy formation and evolution (Frenk & White 2012; Vogelsberger et al. 2014) and it predicts the spectrum of matter fluctuations in the early Universe with exceptional accuracy (Aghanim et al. 2020). However, the absence of experimental evidence of collisionless cold dark matter (CDM) particles (Arcadi et al. 2018), and the fact that N -body simulations based on CDM models presented some discrepancies with observed quantities – such as the missing satellites (Klypin et al. 1999), core-cusp (Moore 1994), diversity (Oman et al. 2015), and Too-Big-To-Fail (Boylan-Kolchin et al. 2011) problems – generated interest in alternative DM models. The inconsistencies between simulations and observations have been in part mitigated with the inclusion of baryonic effects in simulations and with the discovery of new faint satellites in the Milky Way

(Bechtol et al. 2015; Drlica-Wagner et al. 2015). However, it is still uncertain if this is sufficient to bring the simulated CDM predictions completely in agreement with observations or if the discrepancies point us in the direction of a DM model different from CDM (Bullock & Boylan-Kolchin 2017). One possibility, first introduced by Spergel & Steinhardt (2000), is that DM is not collisionless, but has self-interactions in addition to gravity. DM self-interactions can have an impact on the macroscopic characteristics of haloes, alleviating some of the issues that emerge in a collisionless CDM scenario, while leaving the properties on large scale unchanged. In particular, self-interactions can flatten the centrally peaked cusps in the inner regions of galaxies and disturb the growth of dense satellite galaxies, thus potentially solving the core-cusp and too-big-to-fail issues (Vogelsberger et al. 2012; Elbert et al. 2015). Recently, self-interacting dark matter (SIDM) has received new attention thanks to the numerical developments that now allow us to accurately simulate these scenarios, modelling elastic or inelastic particle scattering, constant or velocity-dependent self-interaction cross-section or more exotic variations (Vogelsberger et al. 2012; Rocha et al. 2013; Kaplinghat, Tulin & Yu 2014; Vogelsberger et al. 2016; Sameie et al. 2018; Robertson et al. 2018b; Despali et al. 2019; Kaplinghat, Valli & Yu 2019; Lovell, Zavala & Vogelsberger 2019;

* E-mail: cmastromarino@roma2.infn.it

Vogelsberger et al. 2019; Kaplinghat, Ren & Yu 2020; Sameie et al. 2020; Robertson et al. 2021).

Observational constraints on the self-interaction cross-section can differ significantly, depending on the considered scale. For example, the distribution of DM in dwarf galaxies requires a cross-section $\sigma/m > 0.5 \text{ cm}^2 \text{ g}^{-1}$ (Elbert et al. 2015), while from the ellipticity of elliptical galaxies it was deduced that $\sigma/m \leq 1 \text{ cm}^2 \text{ g}^{-1}$ (Peter et al. 2013a) and strong lensing arc statistics in galaxy clusters allow $\sigma/m < 0.1 \text{ cm}^2 \text{ g}^{-1}$ (Meneghetti et al. 2001). Given these disparities on different scales, a constant cross-section compatible with cluster scale limitations is unable to appreciably lower the central density of dwarf galaxies (Zavala et al. 2013; Fry et al. 2015). As a result, there has been a surge in interest in SIDM models with velocity-dependent cross-sections, that is, a cross-section that decreases with increasing relative velocity of the particles. The effective cross-section in dwarf galaxies can then be several orders of magnitude bigger than in cluster-sized haloes, bringing constraints on different scales into agreement (Zavala & Frenk 2019; Correa 2021; Yang, Nadler & Yu 2023). However, the majority of this prior research has relied on simulations that do not include the physics of baryons (i.e. DM-only simulations.) Recent works are instead starting to model the interplay between self-interactions and baryonic physics, finding that previous predictions based on DM-only simulations need to be updated. At the scale of (massive) galaxies, relevant for our work, Sameie et al. (2018) and Elbert et al. (2018) used simulations of isolated galaxies to show that the cross talk between SIDM and baryons produces a wide range of halo profiles, depending on how centrally concentrated the baryonic component is. Despali et al. (2019) ran full-hydrodynamic zoom-in simulations of nine haloes hosting massive galaxies, finding that SIDM haloes can be both cored and cuspy, depending on halo mass, morphological type, as well as the halo mass accretion history. Moreover, the same simulations show that CDM and SIDM halo shapes are similar when baryons are included (Despali et al. 2022) and thus $\sigma/m = 1 \text{ cm}^2 \text{ g}^{-1}$ is not yet excluded, revising the constraints from Peter et al. (2013a). Robertson et al. (2018a, b, 2021); Shen et al. (2022) have studied the effect of SIDM on the density profiles of galaxy clusters, also concluding that the inclusion of baryons reduces the difference between CDM and SIDM predictions. These results show that the inclusion of baryons in simulations can have a strong impact on the final properties of haloes in SIDM cosmologies, similarly to what has been demonstrated in CDM simulations, meaning that some constraints must be revisited with new more realistic runs.

We choose the mass range of massive galaxies to compare with previous predictions (Despali et al. 2019) and observational results (Auger et al. 2010; Barnabè et al. 2011; Cappellari et al. 2013; Sonnenfeld et al. 2013; Lovell et al. 2018) at the scales of elliptical galaxies. At redshift $z > 0$, elliptical galaxies are the typical strong lenses: gravitational lensing is the most accurate technique to measure the total mass distribution of galaxies and clusters and thus it is especially relevant in the study of alternative DM models. We thus study both the properties of local galaxies at $z = 0$ and of their counterparts at $z = 0.5$ and $z = 1$. In the context of SIDM, some of the most stringent constraints on the self-interaction cross-section (Miralda-Escudé 2002; Peter et al. 2013b) – although revisited adding the effect of baryonic physics by Despali et al. (2022) – have been derived in this regime, given that the masses of lens galaxies can be measured directly. We select haloes hosting massive galaxies ($10^{12} M_{\odot} h^{-1} < M_{200} < 10^{13.5} M_{\odot} h^{-1}$) in a cosmological box from Robertson et al. (2021) to study the interplay between baryonic physics and SIDM and test the results by Despali

et al. (2019) on a much larger sample. We analyse the properties of massive galaxies in three scenarios: the standard CDM and two SIDM models, with a constant cross-section $\sigma/m = 1 \text{ cm}^2 \text{ g}^{-1}$ or a velocity-dependent cross-section. The paper is structured as follows. In Section 2, we describe the simulations and the halo selection. In Section 3, we present our results on the halo density profiles and concentration: we study the structure of haloes, in terms of their total and DM density profiles, we calculate the best fit Einasto parameters and discuss the resulting concentration–mass relations. We then discuss observable properties that could be used to distinguish CDM from the alternative models considered here, that is, DM fractions (Section 4) and the sizes of the strong lensing signal (Section 5). Finally, we summarize our results and draw our final conclusions in Section 6.

2 SIMULATIONS

The simulations used in this work were first presented in Robertson et al. (2021) and are part of the extended family of EAGLE simulations (Schaye et al. 2015). These are cosmological hydrodynamical simulations of galaxy formation run with the GADGET-3 code (Springel 2005) and a galaxy-formation model that includes gas cooling, star formation, and feedback from both stars and active galactic nuclei.

Here we use a set of six runs in total, which simulate the same volume of $V = (50 \text{ cMpc})^3$ (L050N0752) keeping the EAGLE galaxy formation model fixed, but in CDM and two SIDM models: one with constant cross-section $\sigma/m = 1 \text{ cm}^2 \text{ g}^{-1}$ and one with a velocity-dependent cross-section. The simulations follow $N = 75^3$ DM particles and an (initially) equal number of gas particles. The DM mass resolution is $m_{\text{DM}} = 1.43 \cdot 10^7 M_{\odot} h^{-1}$, while the baryonic resolution is $m_g = 2.67 \cdot 10^6 M_{\odot} h^{-1}$. The spatial resolution, that is, the Plummer-equivalent gravitational softening length is $\epsilon = 1.03 \text{ kpc } h^{-1}$. The cosmological parameters derived from the Planck data (Planck Collaboration et al. 2014) are used: $\Omega_m = 0.307$, $\Omega_{\Lambda} = 0.693$, $\Omega_b = 0.0483$, $\sigma_8 = 0.83$, and $h = 0.6777$.

The implementation of DM self-interactions used in the SIDM simulations is presented in Robertson, Massey & Eke (2017) and its integration into the EAGLE simulations discussed in Robertson et al. (2018b). The velocity-dependent cross-section is described by three parameters: the DM mass m_{χ} , the mediator mass m_{ϕ} , and a coupling strength α_{χ} . The model corresponds to DM particles scattering through a Yukawa potential and the differential cross-section is

$$\frac{d\sigma}{d\Omega} = \frac{\alpha_{\chi}^2}{m_{\chi}^2 (m_{\phi}^2/m_{\chi}^2 + v^2 \sin^2(\frac{\theta}{2}))^2}, \quad (1)$$

where v is the relative velocity between two DM particles and θ is the polar scattering angle. By defining $\omega \equiv m_{\phi}c/m_{\chi}$ as a characteristic velocity below which the scattering is roughly isotropic with $\sigma \sim \sigma_0$ and above which the cross-section decreases with increasing velocity, the cross-section can be written as

$$\frac{d\sigma}{d\Omega} = \frac{\sigma_0}{4\pi(1 + \frac{v^2}{\omega^2} \sin^2(\frac{\theta}{2}))^2}. \quad (2)$$

The velocity-dependent model considered here, already used in Robertson et al. (2018b), adopts $m_{\chi} = 0.15 \text{ GeV}$, $m_{\phi} = 0.28 \text{ keV}$ and $\alpha_{\chi} = 6.74 \times 10^{-6}$, corresponding to $\sigma_0 = 3.04 \text{ cm}^2 \text{ g}^{-1}$, $\omega = 560 \text{ km/s}$.

We disentangle the effect of baryons and SIDM by comparing the DM-only and hydrodynamic versions of the same boxes. Throughout the paper, we label the full-hydrodynamic simulations run with a ‘b’ to

Table 1. Number of haloes in the three bins in mass (Low Mass, Intermediate Mass, and High-Mass) in each of the six considered boxes (both DM-only and full-hydrodynamic simulations).

	$\log\left(\frac{M_{200}}{M_{\odot}h^{-1}}\right)$	Low Mass [12,12.5]	Int. Mass [12.5,13]	High Mass [13,13.5]	Tot [12,13.5]
$z = 0$	CDM	99	37	17	153
	CDMb	83	32	14	129
	SIDM1	99	38	17	154
	SIDM1b	83	32	13	128
	vdSIDM	94	38	17	149
	vdSIDMb	87	31	15	133
$z = 0.5$	CDM	112	35	11	158
	CDMb	94	31	10	135
	SIDM1	112	35	11	158
	SIDM1b	96	31	10	137
	vdSIDM	113	34	11	158
	vdSIDMb	94	32	10	136
$z = 1$	CDM	94	31	5	130
	CDMb	80	27	4	111
	SIDM1	95	31	5	131
	SIDM1b	80	28	4	112
	vdSIDM	97	31	5	133
	vdSIDMb	82	28	4	114

distinguish them from their DM-only counterparts: CDM and CDMb, SIDM1 and SIDM1b, vdSIDM and vdSIDMb. These simulations and DM models have already been analysed in Robertson et al. (2021) to look at the density profiles of clusters of galaxies in CDM and SIDM models and in Bondarenko et al. (2021) to analyse how SIDM effects behave over a wide range of mass scales.

2.1 Halo selection

The haloes are identified by SUBFIND, following the Friends-of-Friends (FOF) algorithm, with a linking length of $b = 0.2$ (Davis et al. 1985). We adopt M_{200} as our definition of halo mass (i.e. the corresponding radius R_{200} encloses 200 times the critical density $\rho_c(z)$) and we select systems with masses $10^{12} M_{\odot} h^{-1} < M_{200} < 10^{13.5} M_{\odot} h^{-1}$. Throughout the paper, we split our sample into three mass bins: $12.0 < \log(M_{200}/M_{\odot} h^{-1}) < 12.5$ (Low Mass), $12.5 < \log(M_{200}/M_{\odot} h^{-1}) < 13.0$ (Intermediate Mass), and $13.0 < \log(M_{200}/M_{\odot} h^{-1}) < 13.5$ (High Mass – up to the largest mass found in the box). The number of selected haloes in each mass bin and simulation is listed in Table 1. Fig. 1 shows the galaxy properties of the considered sample at $z = 0$ in the $M_* - r_{\text{eff}}$ plane, together with the sample simulated in Despali et al. (2019), demonstrating the extended statistics of this work.

We study the summary properties of haloes, but we also compare individual systems to their counterparts across models. In order to identify the same objects in the six boxes, we match the position of the centre of mass of each halo. We check that the distance between the matched haloes is smaller than their virial radius, that is, $d_{\text{min}}/r_{\text{vir}} < 1$. Fig. 2 shows the masses of matched haloes at $z = 0$. Most of the haloes are distributed on the bisector, showing that corresponding systems have comparable masses and that matches have been correctly identified.

3 HALO PROFILES AND CONCENTRATIONS

In this Section, we measure the density profiles and concentrations of the haloes in all runs and discuss the impact of SIDM and baryons.

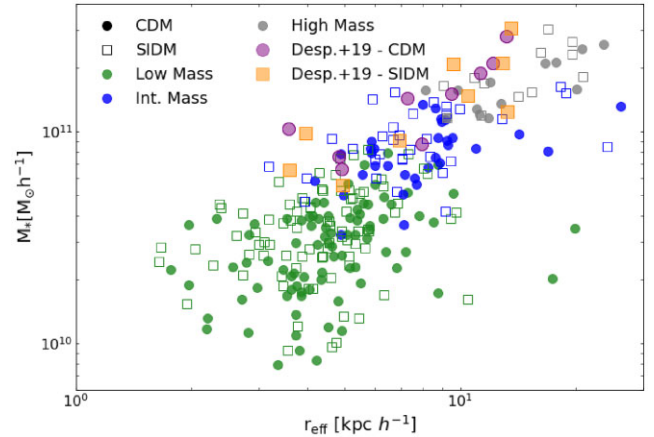


Figure 1. Total stellar mass as a function of the effective radius of the central galaxy for the considered sample of haloes in the hydrodynamic runs at $z = 0$. We compare them with the galaxies simulated (at $z = 0.2$) by Despali et al. (2019). The distribution at the other two considered redshifts ($z = 0.5, 1$) is similar. The effective radius is calculated as the radius enclosing half of the stellar mass.

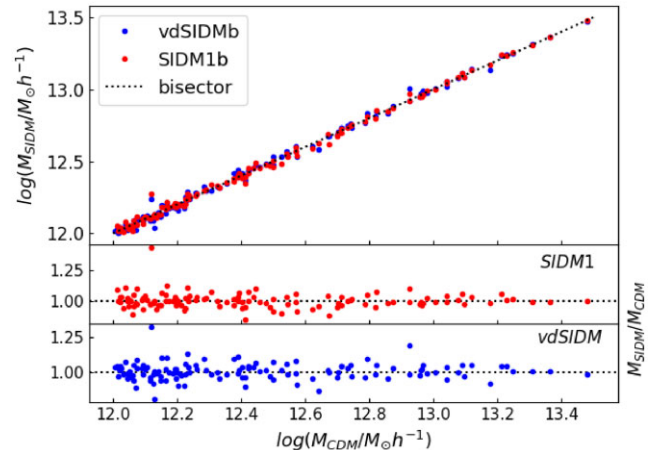


Figure 2. Top panel: masses of matched systems in full-hydrodynamic simulations at $z = 0$; in blue matched system between CDMb and vdSIDMb, in red matched systems between CDMb and SIDM1b. The black dotted line represents the bisector. Central panel: $M_{\text{SIDM1b}}/M_{\text{CDMb}}$. Bottom panel: $M_{\text{vdSIDMb}}/M_{\text{CDMb}}$.

The influence of self-interactions on DM density profiles has been the driving force behind the field: the primary signature of SIDM is a decrease in the DM density in the central regions of haloes, due to the formation of a core. However, previous works have demonstrated that this effect can be mitigated or even reversed in the presence of a dense baryonic component (Sameie et al. 2018; Despali et al. 2019) and in the event of gravitational core-collapse.

3.1 Method

We calculate the spherically averaged total and DM density profiles of individual haloes in each of the six runs (see Section 2). We compute the density ρ_i in 30 logarithmically spaced spherical shells in the radial range from $r = 1 \text{ kpc } h^{-1}$ to the mean R_{200} of each mass bin. The softening length of the simulations ($\epsilon = 1.03 \text{ kpc } h^{-1}$) is similar to the minimum considered radius.

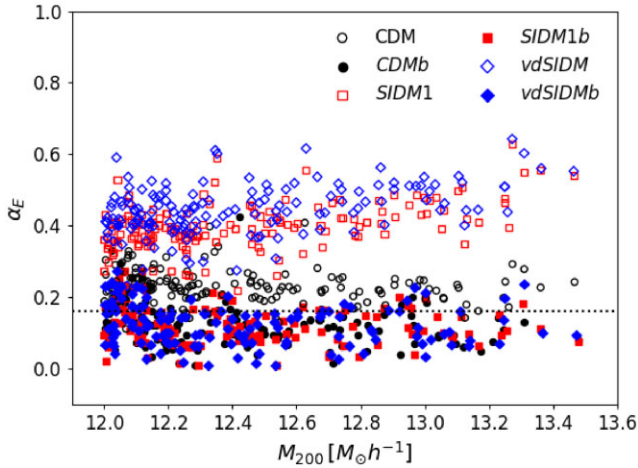


Figure 3. The Einasto shape parameter α_E for individual simulated haloes in different simulations. The empty points represent the best fit values for DM-only runs with each DM model, while the filled points correspond to the full-hydrodynamic simulations. The horizontal dotted line is fixed at $\alpha_E = 0.16$.

We test four different fitting formulae, namely NFW (Navarro et al. 1997), Einasto (Einasto 1965), Burkert (Burkert 1995), and Zavala (Zavala et al. 2013) profiles – the latter is similar to the Burkert profile but with two scale radii. In the DM-only version, the standard NFW profile cannot reproduce cored profiles, while the SIDM haloes are well described by profiles explicitly characterized by a core radius as the Burkert profile or the three-parameter formula defined by Zavala et al. (2013). In hydro runs, the Zavala profile is a good fit for SIDM haloes, while the Burkert profile fails to reproduce the cuspy density distribution. We find that the Einasto profile can instead well describe all our runs. This is defined as

$$\rho(r) = \rho_{-2} \exp \left\{ -\frac{2}{\alpha_E} \left[\left(\frac{r}{r_{-2}} \right)^{\alpha_E} - 1 \right] \right\}, \quad (3)$$

where r_{-2} and ρ_{-2} are respectively the radius and the density at which $\rho(r) \propto r^{-2}$, while α_E is the shape parameter. For this reason, in the rest of this work, we present results calculated with the Einasto profile only, leaving a more detailed discussion of the other fitting formulae to Appendix A. In particular, we fit both the average profiles and each individual halo and we calculate the halo concentration as $c_{200} = r_{200}/r_{-2}$.

3.2 Individual density profiles

For each halo, we perform the Einasto fit twice, both leaving the shape parameter free to vary and fixing it to a given value of $\alpha_E = 0.16$, as proposed in previous works (Springel et al. 2008). The Einasto profile with $\alpha_E = 0.16$ is a good fit to CDM haloes and all full-hydro runs, but it fails to reproduce the central core the DM-only SIDM runs, generating exceedingly large scale radii. Fig. 3 shows the distribution of the best fit values of α_E as a function of mass for haloes at $z = 0$. In the DM-only runs, α_E is higher in SIDM1 and vdSIDM (red and blue empty squares) than in CDM (black empty circles), due to the presence of the central core. Instead, when baryons are included the best fit values are similar in all models (black, blue, and red filled symbols) and closer to $\alpha_E = 0.16$: this means that in presence of the baryonic component an Einasto profile with only two free parameters can be used, reducing the number of parameters of the fit.

This result is interesting in comparison to the profiles analysed by Eckert et al. (2022), who performed a similar analysis on the BAHAMAS-SIDM cluster-scale simulations (McCarthy et al. 2016; Robertson et al. 2018a). For $M_{200} > 10^{14} M_\odot$ and for the same self-interacting model with constant cross-section, they found a higher $\alpha_E \sim 0.4$, while only a lower cross-section $\sigma/m = 0.1 \text{ cm}^2 \text{ g}^{-1}$ is required to have the same slope as in CDM at these scales.

3.3 Mean density profiles

We start from the haloes at $z = 0$ and for each mass bin we calculate the best-fitting Einasto profile on the mean density profile. This is explicitly computed as the sum of the density on the same spherical shell of each halo, divided by the number of haloes in the respective mass bin. The Einasto best fit parameters for the mean density profile, found as the values that minimize the sum of the squared residuals of $\log(\rho_{\text{model}}) - \log(\rho_i)$, and related uncertainties can be found in Table 2.

The results are shown in Fig. 4 for all models: CDM in black, SIDM1 in red, and vdSIDM in blue. Here we show the total density profile, including both the baryonic and DM components in the full-hydro runs. Each column shows the results for a given mass bin, with solid (dashed) lines standing for full-hydro (DM-only) runs. In the residual panels we plot the ratio between the SIDM and CDM profiles in each run. Finally, the gray shaded region represents the 1σ uncertainty on the ratio between the stacked profiles.

In DM-only simulations, we recover the well-known trend of SIDM1 (and vdSIDM) haloes forming a central core: the central density ($r \leq 10 \text{ kpc } h^{-1}$) is lower by 50 per cent or more compared to the CDM case. In the full-hydro runs, the presence of baryons counteracts the core formation. Given that this effect is stronger for SIDM, baryonic physics almost erases the differences between CDM and SIDM total profiles, as can be seen by comparing the two residual panels of each case in Fig. 4. The effect is analogous at higher redshift – see the coloured curves again in the residual panels, representing haloes at $z = 0.5$ (green) and $z = 1$ (purple). The ratios at different redshifts remain almost constant: the effects of self-interactions are almost redshift-independent, in all runs, suggesting that they depend primarily on halo mass and not on redshift.

Our results point in the same direction as previous studies (Sameie et al. 2018; Despali et al. 2019; Robertson et al. 2021) and can be understood by considering that $M \sim 10^{13} M_\odot h^{-1}$ corresponds to the halo mass in which star formation is most efficient, baryons dominate the inner density profile and the DM nature plays a secondary role.

Despite this, we find a weak trend with mass

(i) **Low Mass** ($\log [M_{200}/M_\odot h^{-1}] \in [12.0, 12.5]$): the SIDM1b and vdSIDMb profiles have a *higher* density than that of CDMb ($\rho_{\text{SIDM}}/\rho_{\text{CDM}} > 1$) in the central regions. However, the difference between the two models drops to less than 20 per cent.

(ii) **Intermediate Mass** ($\log [M_{200}/M_\odot h^{-1}] \in [12.5, 13.0]$): the difference between the density profiles disappears and the profiles are almost exactly overlapping ($\rho_{\text{SIDM}}/\rho_{\text{CDM}} \sim 1$).

(iii) **High Mass** ($\log [M_{200}/M_\odot h^{-1}] \in [13.0, 13.5]$): the situation is reversed and the profiles of SIDM1b and vdSIDMb have a *lower* density than the profile of CDMb ($\rho_{\text{SIDM}}/\rho_{\text{CDM}} < 1$), but also for this mass bin the difference between the two DM models is less than 20 per cent.

The trend with mass mentioned earlier is weaker than that reported by Despali et al. (2019), who found steeper SIDM profiles at $M_{200} \sim 10^{12.5} M_\odot h^{-1}$ than we do here. Given the halo-to-halo variations of the density profiles, our larger statistics allows us to better capture

Table 2. Best fit parameters with Einasto profile for the three mass bins at $z = 0$, for each simulation: ρ_{-2} is expressed in $M_{\odot} h^{-1}/(\text{kpc}/h)^3$, r_{-2} in $\text{kpc} h^{-1}$, and α_E is dimensionless. The errors represent 1 standard deviations.

		Low mass	Intermediate mass	High mass
CDM	ρ_{-2}	$(4.34 \pm 0.66) \cdot 10^6$	$(3.90 \pm 0.72) \cdot 10^6$	$(2.32 \pm 0.34) \cdot 10^6$
	r_{-2}	19.96 ± 1.51	30.73 ± 2.68	51.68 ± 3.23
	α_E	0.26 ± 0.02	0.28 ± 0.03	0.23 ± 0.02
CDMb	ρ_{-2}	$(1.31 \pm 0.39) \cdot 10^7$	$(7.44 \pm 2.36) \cdot 10^6$	$(3.60 \pm 1.06) \cdot 10^6$
	r_{-2}	11.18 ± 1.75	20.51 ± 3.32	38.01 ± 5.29
	α_E	0.15 ± 0.02	0.14 ± 0.03	0.12 ± 0.02
SIDM1	ρ_{-2}	$(2.42 \pm 0.33) \cdot 10^6$	$(1.87 \pm 0.27) \cdot 10^6$	$(1.21 \pm 0.14) \cdot 10^6$
	r_{-2}	28.13 ± 1.75	47.85 ± 2.80	81.58 ± 3.52
	α_E	0.39 ± 0.03	0.46 ± 0.04	0.47 ± 0.03
SIDM1b	ρ_{-2}	$(1.89 \pm 0.67) \cdot 10^7$	$(7.35 \pm 2.18) \cdot 10^6$	$(2.41 \pm 0.70) \cdot 10^6$
	r_{-2}	9.56 ± 1.75	20.97 ± 3.18	46.34 ± 6.21
	α_E	0.14 ± 0.02	0.15 ± 0.02	0.13 ± 0.02
vdSIDM	ρ_{-2}	$(2.04 \pm 0.28) \cdot 10^6$	$(1.61 \pm 0.22) \cdot 10^6$	$(1.12 \pm 0.14) \cdot 10^6$
	r_{-2}	31.09 ± 1.84	52.13 ± 2.88	85.70 ± 3.77
	α_E	0.43 ± 0.04	0.50 ± 0.04	0.50 ± 0.03
vdSIDMb	ρ_{-2}	$(1.91 \pm 0.67) \cdot 10^7$	$(8.48 \pm 2.84) \cdot 10^6$	$(2.37 \pm 0.67) \cdot 10^6$
	r_{-2}	9.42 ± 1.72	19.66 ± 3.4	45.98 ± 6.00
	α_E	0.14 ± 0.02	0.16 ± 0.03	0.13 ± 0.02

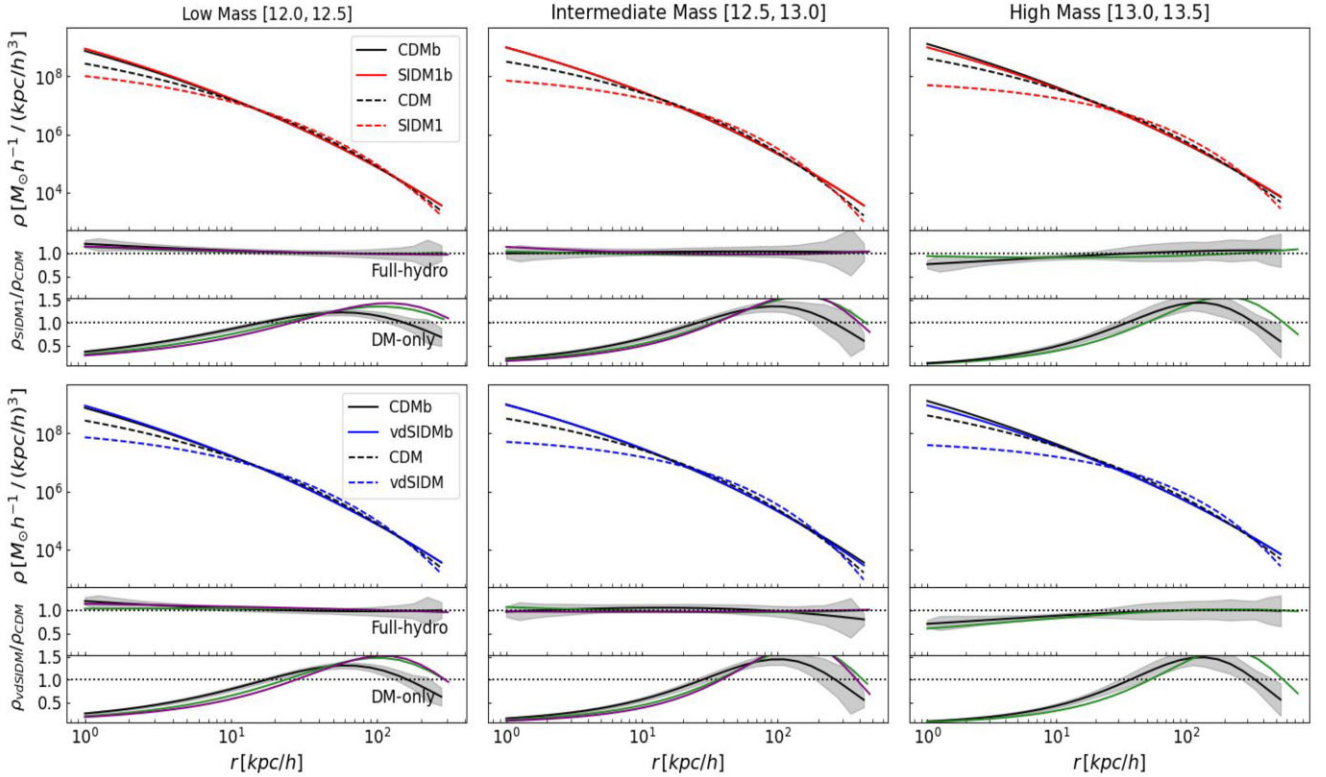


Figure 4. Top: fit of the total density profiles with CDM and SIDM1 models for both DM-only (dashed lines) and full-hydrodynamic (solid lines) simulations, at $z = 0$. The fit is performed on the mean profile of each bin. Bottom: ratio between the two models for the total and the DM-only profiles: $\rho_{\text{SIDM}}/\rho_{\text{CDM}}$. Each colour represent the ratio between the profiles at different redshifts: black for $z = 0$, green $z = 0.5$, and purple for $z = 1$. For the High Mass bin, we do not show the profiles at $z = 1$, since we do not have enough haloes to perform a robust fit. The gray shaded regions show the 1σ uncertainties calculated on each mass bin and propagated on the ratios between the stacked profiles at $z = 0$. The first density value is calculated at $r = 1 \text{ kpc} h^{-1}$, therefore similar to the spatial resolution (softening length $\epsilon = 1.03 \text{ kpc} h^{-1}$). The mass bins are (columns from left to right), Low Mass: $\log(M_{200}/M_{\odot} h^{-1}) \in [12.0, 12.5]$, Intermediate Mass: $\log(M_{200}/M_{\odot} h^{-1}) \in [12.5, 13.0]$, and High Mass: $\log(M_{200}/M_{\odot} h^{-1}) \in [13.0, 13.5]$.

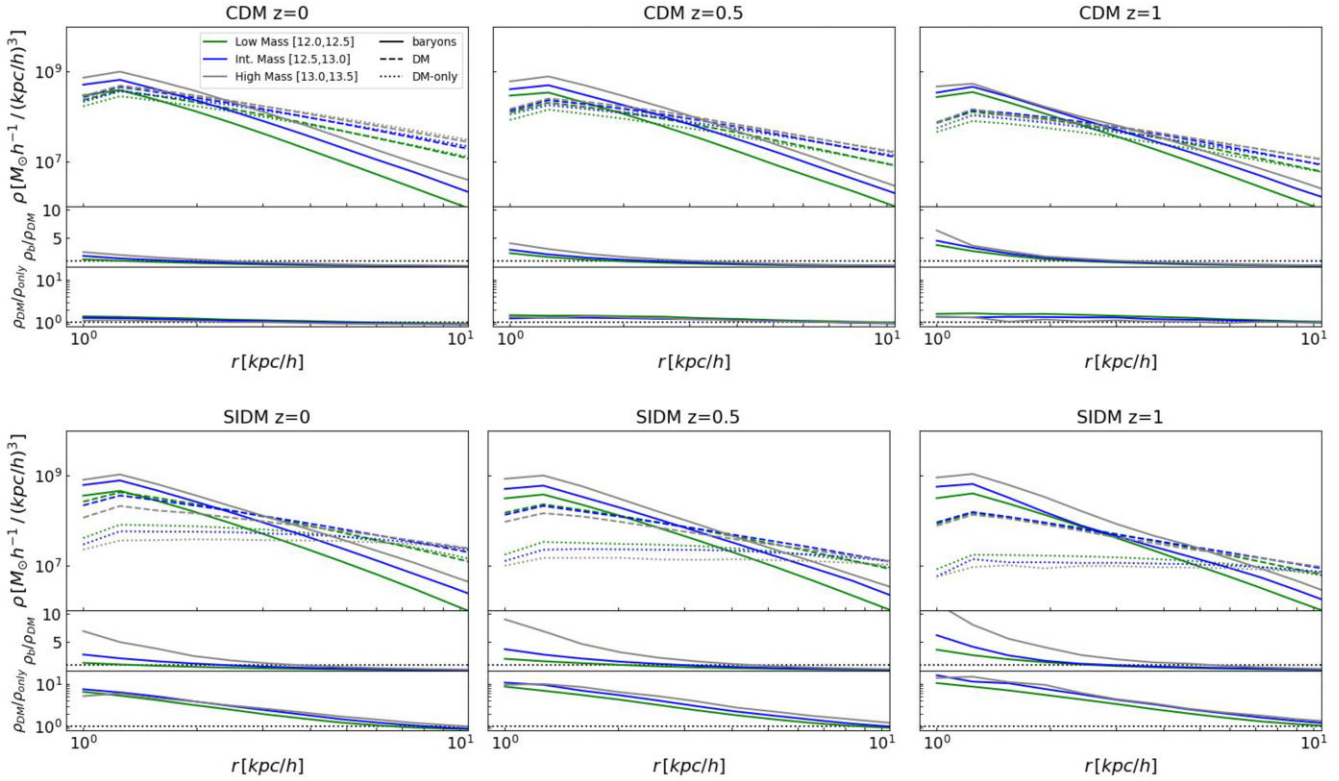


Figure 5. Zoom of the central region ($r \leq 10 \text{ kpc } h^{-1}$) of the baryonic (solid lines) and DM mean density profiles, for both full-hydro (dashed lines) and DM-only (dotted lines) runs at three different redshift for CDM (top row) and SIDM1 (bottom row). Different colour refer to the different mass bins. The middle panels show the ratio between the baryon density and DM density in full-hydro simulations (ρ_b/ρ_{DM}). The bottom panels show the ratio between the DM components in full-hydro and DM-only runs (ρ_{DM}/ρ_{only}).

the properties of the entire population and avoid selection biases that can affect small samples. We also point out that the interplay between baryons could be different when using the EAGLE (as we do here) or TNG (as in Despali et al. 2019) galaxy formation models, causing systematic differences between the results.

In order to better understand the origin of the similarity between the profiles, we now analyse the profiles of DM and baryons in Fig. 5. The Figure shows the evolution with redshift of inner part of the baryonic (solid lines) and DM mean density profiles, for both full-hydro (dashed lines) and DM-only (dotted lines) runs. The middle panels show the ratio between the baryon density and DM density in full-hydro simulations (ρ_b/ρ_{DM}). In CDM we find that the ratios of the three mass bin follow the same evolution with redshift leading to the final cuspy profile at $z = 0$ independently of the halo masses. In SIDM, while the Low Mass bin behaves similarly to the CDM case, the ratios for the Intermediate Mass bin and even more for the High Mass bin have higher values than CDM and a steep increase with redshift. These results can be related to the formation history of the halo as it has been done in Despali et al. (2019). The Low Mass haloes form at higher redshift and the self-interactions started to act at earlier time, but then the baryons dominate the evolution of the density profile and the interplay between baryons and DM leads to the final cuspy profile, acting similarly as in CDM scenario. Alternatively, the High Mass haloes formed at lower redshift and thus we see them at the stage in which the self-interaction is acting in the central regions, leading to lower DM density than for the Low Mass haloes, thus higher ratios.

The bottom panels show instead the ratio between the DM components in full-hydro and DM-only runs (ρ_{DM}/ρ_{only}). We find

that the presence of a central baryonic component contracts the halo in the inner region in both models, however while in CDM $\rho_{DM}/\rho_{only} \sim 1.5$, the effect is much stronger in SIDM with $\rho_{DM}/\rho_{only} > 5.0$.

This last result clarifies why the density profile in the full-hydro runs are similar to each other, while it is the connection between halo mass and formation history that explains the trend with mass that we found here.

3.4 Concentration–mass relation

The profiles of individual systems can deviate from the mean profiles shown in Fig. 4: the halo-to-halo variation can be characterized by means of the distribution of halo concentrations (Navarro et al. 1997; Duffy et al. 2008; Dutton & Maccio 2014; Schaller et al. 2015). We now use the fits to individual haloes to calculate the distribution of concentrations. We then define the concentration–mass ($c - M$) relation as

$$\log(c_{200}) = A - B \log(M_{200}/M_{\odot} h^{-1}), \quad (4)$$

and find the best fit values (A, B) for each considered model. These are listed in Table 3, together with their 1σ uncertainties. We plot the best fit concentration–mass relations for each considered model and redshift in Fig. 6. In the DM-only runs, the three $c - M$ relations are essentially parallel to each other: the core creation induced by self-interactions reduces the halo concentration similarly for all haloes. This is expected, given that the concentration is potentially ill-defined for cored profiles, where the core in practice modifies the location of r_{-2} . However, this does not affect the hydro runs, given that the profiles are similar to the CDM model. In this case, although the

Table 3. The linear best fit parameters of concentration–mass relations for each model at different redshifts: $\log(c_{200}) = A - B \log(M_{200})$. See also Fig. 6.

		$z = 0.0$	$z = 0.5$	$z = 1.0$
CDM	A	2.42 ± 0.22	2.04 ± 0.54	2.70 ± 0.53
	B	0.11 ± 0.02	0.08 ± 0.04	0.14 ± 0.04
CDMb	A	5.91 ± 0.39	9.27 ± 2.18	18.14 ± 2.61
	B	0.37 ± 0.06	0.67 ± 0.16	1.2 ± 0.2
SIDM1	A	2.56 ± 0.11	2.05 ± 0.28	2.15 ± 0.30
	B	0.13 ± 0.01	0.10 ± 0.02	0.11 ± 0.02
SIDM1b	A	8.23 ± 0.53	13.01 ± 2.72	23.35 ± 7.56
	B	0.55 ± 0.04	0.94 ± 0.21	1.77 ± 0.60
vdSIDM	A	2.24 ± 0.09	1.75 ± 0.24	1.61 ± 0.30
	B	0.11 ± 0.01	0.08 ± 0.02	0.07 ± 0.02
vdSIDMb	A	9.34 ± 0.99	12.20 ± 1.63	26.59 ± 5.97
	B	0.63 ± 0.08	0.87 ± 0.13	2.04 ± 0.47

scatter in the relations is higher than in the DM-only runs (shaded regions in Fig. 6), the SIDMb $c - M$ relations are instead steeper than in CDMb: haloes show a greater diversity of profiles and the $c - M$ trend is consistent with the trend in mass described in Section 3.3. Measuring the $c - M$ relation over a larger range in mass and in a larger simulation box will be essential to confirm this difference in slope.

For comparison, the concentration–mass relation of Dutton & Maccio (2014), based on DM-only simulations of a Λ CDM model with the same cosmological parameters as ours (Planck Collaboration

et al. 2014), is shown as a green solid line in Fig. 6. Covering a wide-mass range $10^{10} \leq M/M_{\odot} h^{-1} \leq 10^{15}$ and fitting an Einasto model to estimate the concentration, they obtained $[A, B] = [2.48, 0.12]$, $[2.29, 0.12]$, and $[1.97, 0.10]$, for $z = 0$, $z = 0.5$, and $z = 1$, respectively. Although these results differ slightly from ours due to the different mass range and the different radial ranges used to perform the fits, they are consistent, within 1σ , with the CDM concentration–mass relation that we find here.

4 DM FRACTIONS

A direct consequence of the different composition of the central part of haloes is a systematic difference in the DM fraction, that can be lower in self-interacting models with respect to CDM. In this section, we attempt a comparison of the simulated DM fractions with observational results and we discuss the possibility of using observed fractions to discriminate between the DM models considered here. We find that there are no substantial differences between the two simulated SIDM models over the halo mass range considered here. This is due to the functional form of the velocity-dependent cross-section, which produces $\sigma/m \sim 1 \text{ cm}^2 \text{ g}^{-1}$ for $M \sim 10^{13} M_{\odot} h^{-1}$ (see Robertson et al. 2021, for more details). For this reason, in the remainder on this work we show results only for the CDM and SIDM1 models.

Previous numerical works (e.g. Lovell et al. 2018) have calculated the DM fraction, or conversely the baryon fraction, in the central regions of simulated haloes and compared it to observational results from lensing (Auger et al. 2010; Barnabè et al. 2011; Sonnenfeld

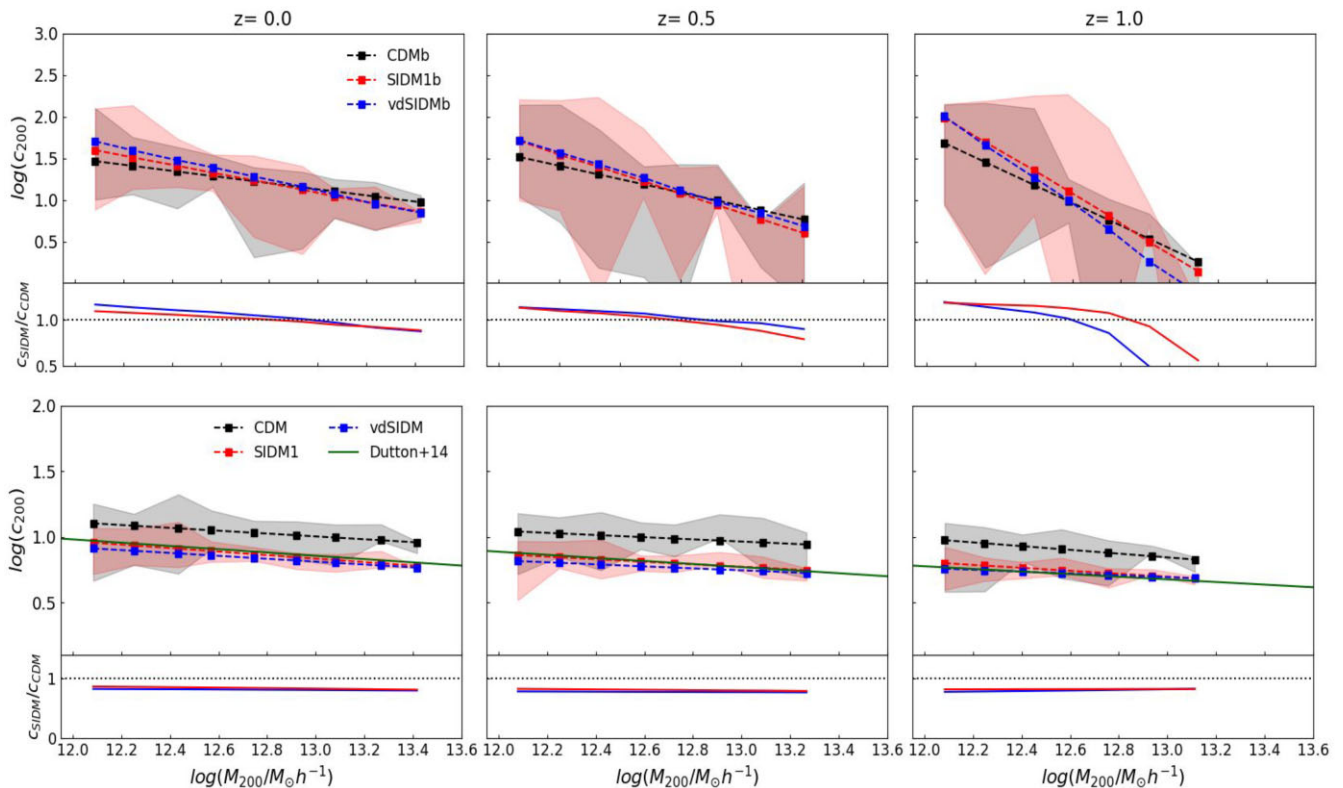


Figure 6. Concentration–mass relation at $z = 0, 0.5$ and 1 (panels from left to right). Top row: full-hydro simulations. Bottom row: DM-only simulations. The black, red, and blue dashed lines show the best-fitting relation for the CDM, SIDM, and vdSIDM runs, respectively. The best fit has been performed on the stacked values over different bins in mass (each containing at least two haloes). The shaded regions show the scatter in each of these bins (the vdSIDM scatter is not shown since it is similar to SIDM1). The solid green lines are the best fit relation from Dutton & Maccio (2014). Bottom subpanels: ratio between the SIDM models and CDM model $c_{\text{SIDM}}/c_{\text{CDM}}$ for both full-hydro and DM-only relations.

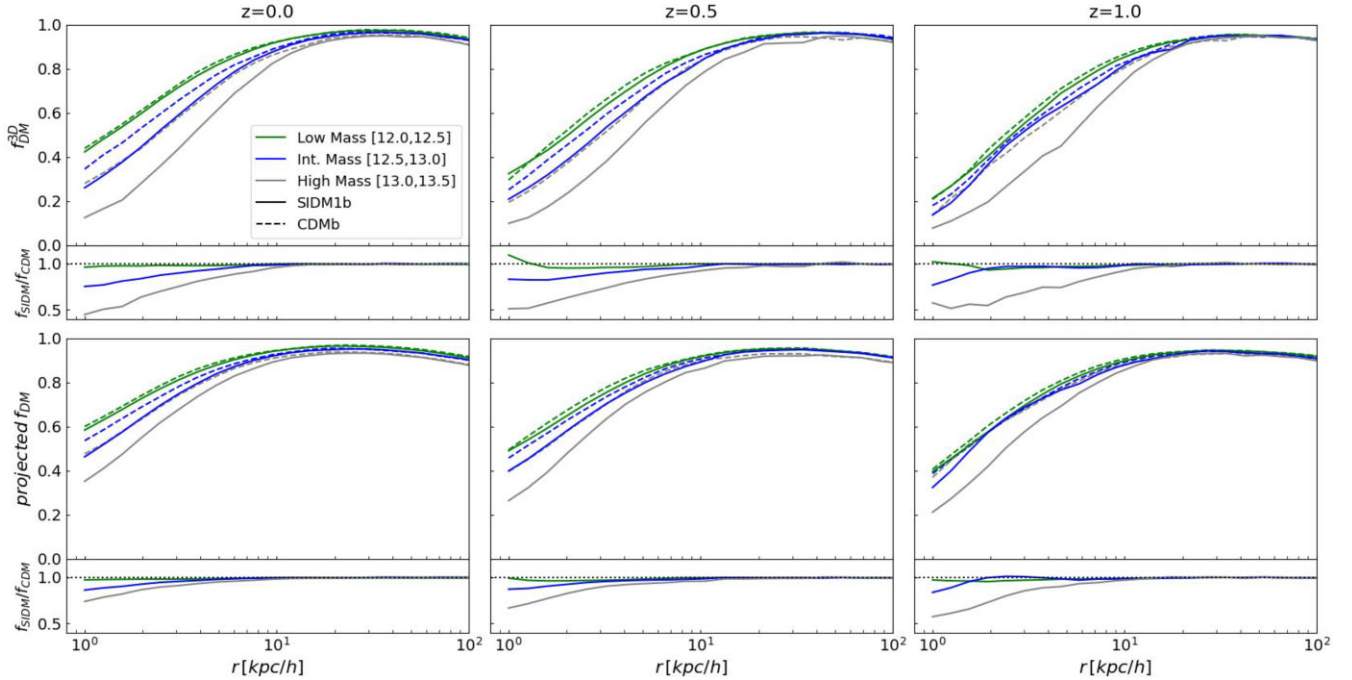


Figure 7. Fraction of enclosed DM mass, f_{DM} , as a function of radius, for each mass bin (different colours) and for the CDMb (solid lines) and SIDM1b (dashed lines) runs. Results for $z = 0$, $z = 0.5$, and $z = 1$ are shown from left to right. Top panels: intrinsic 3D DM fraction. Bottom: projected DM fraction, calculated by averaging over three different viewing angles for each halo. For each angle we measure the DM fraction in concentric cylindrical coronae.

et al. 2013), Jeans modelling (Tortora et al. 2012), and survey data (Cappellari et al. 2013), among others. Observed DM fractions span a wide range of values, depending on the methods and models used to derive them, and they can appear inconsistent with predictions from numerical simulations and with each other. This could be due to a number of reasons, including the details of the IMF model, and the techniques and apertures used for the measurements: it can thus be tricky to reproduce exactly the same measurement procedures in simulations and observations. Moreover, simulated values also strongly depend on the adopted galaxy formation model and on its impact in the inner region of the halo. However, another possibility is that DM models different from CDM could be a better match to observational measurements. Here we test this hypothesis for the case of SIDM1: even in the presence of a bias between observed and simulated fractions, we want to test if simulated CDMb and SIDM1b values follow a different distribution. In this respect, it is less important to demonstrate that simulated fractions exactly reproduce the observed distribution, and instead we search for systematic differences between CDM and SIDM1 simulated values.

We calculate the intrinsic 3D and projected DM fractions f_{DM} as a function of distance from the halo centre for the two hydro runs (i.e. CDMb and SIDM1b) and the three considered redshifts. In projection, we use the DM fraction calculated within concentric cylindrical coronae, over three viewing angles for each halo to increase our statistics. The mean f_{DM} profiles are shown in Fig. 7, directly paralleling the profiles from Fig. 5. While for the Low Mass bin, CDMb, and SIDM1b predictions are in practice identical, the highest-mass haloes show central fractions 50 per cent lower in SIDM1b than CDMb. These results together with what we found in Section 3.3 are showing that, although the total density profile are almost identical, the DM and baryonic distributions differ between models and follow a different evolution with redshift. This highlights the necessity of methods able to distinguish between DM

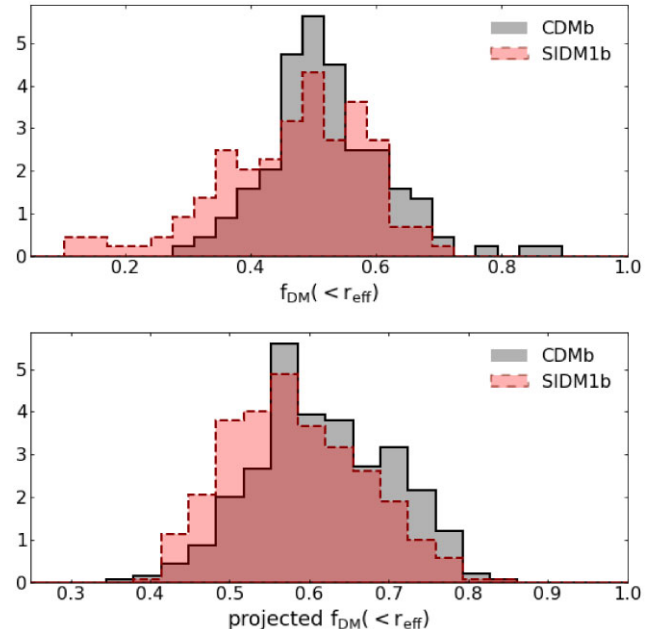


Figure 8. Normalized distribution of simulated DM fractions in the CDMb and SIDM1b models. In the top panel, we show the 3D DM fraction f_{DM} within the effective radius r_{eff} , at $z = 0$, while in the bottom panel we show instead the *projected* DM fraction at $z = 0.5$.

and baryonic components in galaxies and clusters, to discriminate between CDM and SIDM.

However, the difference is significant only in the inner ~ 10 kpc and less pronounced in projection (bottom panels). To quantify the effect on a scale that is common in observational studies, in Fig. 8

we plot the normalized distribution of 3D (top panel) and projected (bottom panel) DM fraction calculated within the effective radius of the central galaxies r_{eff} , defined as the radius that contains half of the stellar mass. In the simulations, this is simply done considering the star particles, while observations rely on the galaxy light to measure the effective radius. In Fig. 8 we notice a shift between the two distributions, with self-interactions causing a more important tail at low fractions and, consequently, a deficit of high values, both in 3D and in projection.

In Fig. 9, we then compare the same DM fractions to previous results, by plotting them as a function of the stellar mass of the central galaxy. In the top panel we show instead the *projected* DM fractions at $z = 0.5$, that is, calculated inside a cylinder of aperture r_{eff} . In this case, for each simulated halo we use three projections that we treat as independent measurements. We compare these values to equivalent measurements in two samples of gravitational lenses: the SLACS (Auger et al. 2010, green stars) and the SL2S (Sonnenfeld et al. 2013, blue triangles) lenses. In the bottom panel, we plot the 3D fractions f_{DM} calculated at $z = 0$ within the effective radius r_{eff} as a function of stellar mass M_* from the CDMb (black dots) and SIDM1b (red squares) runs. The green solid line (and band) shows the results obtained for bulge-dominated galaxies by Lovell et al. (2018) with the IllustrisTNG runs (here we do not reproduce the same selection based on galaxy type). The different trend in our simulated values and the TNG runs is due to the different ways in which the galaxy formation model influences the inner parts of the halo: for example Lovell et al. (2018) finds that the fraction within 5 kpc decrease with increasing halo mass, while this is not the case for the fraction within the effective radius. We then plot observational values obtained from (i) the analysis of the SLACS sample of gravitational lenses at $z < 0.3$ (Barnabè et al. 2011, yellow triangles), (ii) dynamical modelling (Tortora et al. 2012, green dashed line), and (iii) elliptical $z = 0$ galaxies from the ATLAS^{3D} survey (Cappellari et al. 2013, blue stars).

From the mean fractions (black and red lines in both main panels), we notice a different trend of the $f_{\text{DM}} - M_*$ relation: self-interactions produce lower DM fractions at the high mass end, and the trend is reversed at low masses. This is consistent with the mass-dependent differences in the density profiles and in the DM fraction profiles, seen in Section 3. In projection (bottom panel), the difference between the two is smaller and the mean f_{DM} is somewhat flatter.

Finally, the two right panels of Fig. 9 show the normalized distribution of the DM fractions, comparing simulations and observations in order to point out sample differences. While the lens sample from Auger et al. (2010) is consistent with the simulated fractions, Sonnenfeld et al. (2013) and – especially – Cappellari et al. (2013) derived much lower DM fractions. It is difficult to reproduce exactly the distribution measured in observations: possible sources of bias include the sample selection, the difference between the true value of r_{eff} known from simulations and the equivalent measurement from the data, or the spread in redshift of the observed data points. Nevertheless, it is clear that the scatter of observed data points is larger than that produced by the different DM models: a signature of self-interactions on DM fractions exists, but a more detailed evaluation of the observational biases would be required to reach a definitive conclusion.

With our measurements, we show that self-interacting models can produce lower DM fractions at the high mass end, widening the predicted distribution of f_{DM} . However, we do not predict values as low as some of the observations and thus the difference has to be searched elsewhere, that is, in biases between predicted and observed quantities or in more extreme alternative DM models. If these were resolved and measurements were more precise, the offset between

the f_{DM} distributions (Fig. 8) could be used to discriminate between CDM and alternative SIDM models.

5 STRONG LENSING EFFECT

We now investigate the effect of SIDM on the lensing properties of simulated haloes. Gravitational lensing is one of the most accurate techniques to measure the total mass of galaxies and clusters, as well as their radial distribution. The effect of warm or self-interacting DM on the mass distribution and thus on the lensing signal of haloes and subhaloes has been studied in previous works (Robertson et al. 2018a; Despali et al. 2020; Gilman et al. 2020; Hsueh et al. 2020). However, the larger number of haloes available in the runs used here gives us a chance to derive more precise predictions for the population of massive galaxies.

Starting from the particle distribution, we create 2D maps of the projected mass distribution using the library Py-SPHViewer (Benitez-Llambay 2015), as done by Meneghetti et al. (2020) (see also Meneghetti et al. 2022). From these, we calculate the lensing convergence κ – the Laplacian of the lensing potential – with the PyLensLib library (Meneghetti 2021). The value of the lensing convergence determines by how much the background sources appear magnified on the lens plane. In practice, the convergence is defined as a dimensionless surface density and so effectively corresponds to a scaled projected mass density, characterizing the lens system. It can be written as

$$\kappa(x) = \frac{\Sigma(x)}{\Sigma_{\text{crit}}}, \quad \text{with} \quad \Sigma_{\text{crit}} \equiv \frac{c^2}{4\pi G} \frac{D_S}{D_{LS}D_L}, \quad (5)$$

where Σ_{crit} is the critical surface density and D_L , D_S , and D_{LS} stand for the angular diameter distance to the lens, to the source, and between the lens and the source, respectively. Finally, as an estimate of the lensing power of each halo, we calculate the size of the largest critical curve of each system, that is, the region of the plane where the magnification is formally infinite, corresponding to the region where the lensed images form. A massive galaxy can have more than one primary critical line if the system is composed of multiple mass components. Our criterion to identify the primary critical lines is based on the size of the effective Einstein radius: given a critical line enclosing the area A_c , the Einstein radius can be calculated as $\theta_E = \sqrt{A_c/\pi}$.

We repeat this process for all runs using three projections per halo (the same used to calculate the projected DM fractions), in order to increase the sample size. The resulting distributions of Einstein radii θ_E are shown in Fig. 10: in the two panels, we show the results of two different choices of lens and source redshift that reproduce common observed galaxy–galaxy lensing configurations. The haloes used to create the lensing convergence have been selected from the snapshot that correspond to the lens redshift, while the source redshift is used in the calculation of D_S and D_{LS} and thus influences the convergence.

From the distributions, it is clear how the similarity between the halo profiles in the hydro runs propagates into similarities in their lensing properties, in comparison to the DM-only runs (empty dashed histograms). Counter-intuitively, a small shift between the two distributions can be seen (especially in the right hand panel), producing a lack of small Einstein radii in SIDM1. This fact is a result of the different slope of the concentration–mass relations: the least massive haloes in our sample are more concentrated in SIDM1b than in CDMb and thus produce a stronger lensing effect. However, this does not influence the high- θ_E end of the distribution, dominated by massive galaxies.

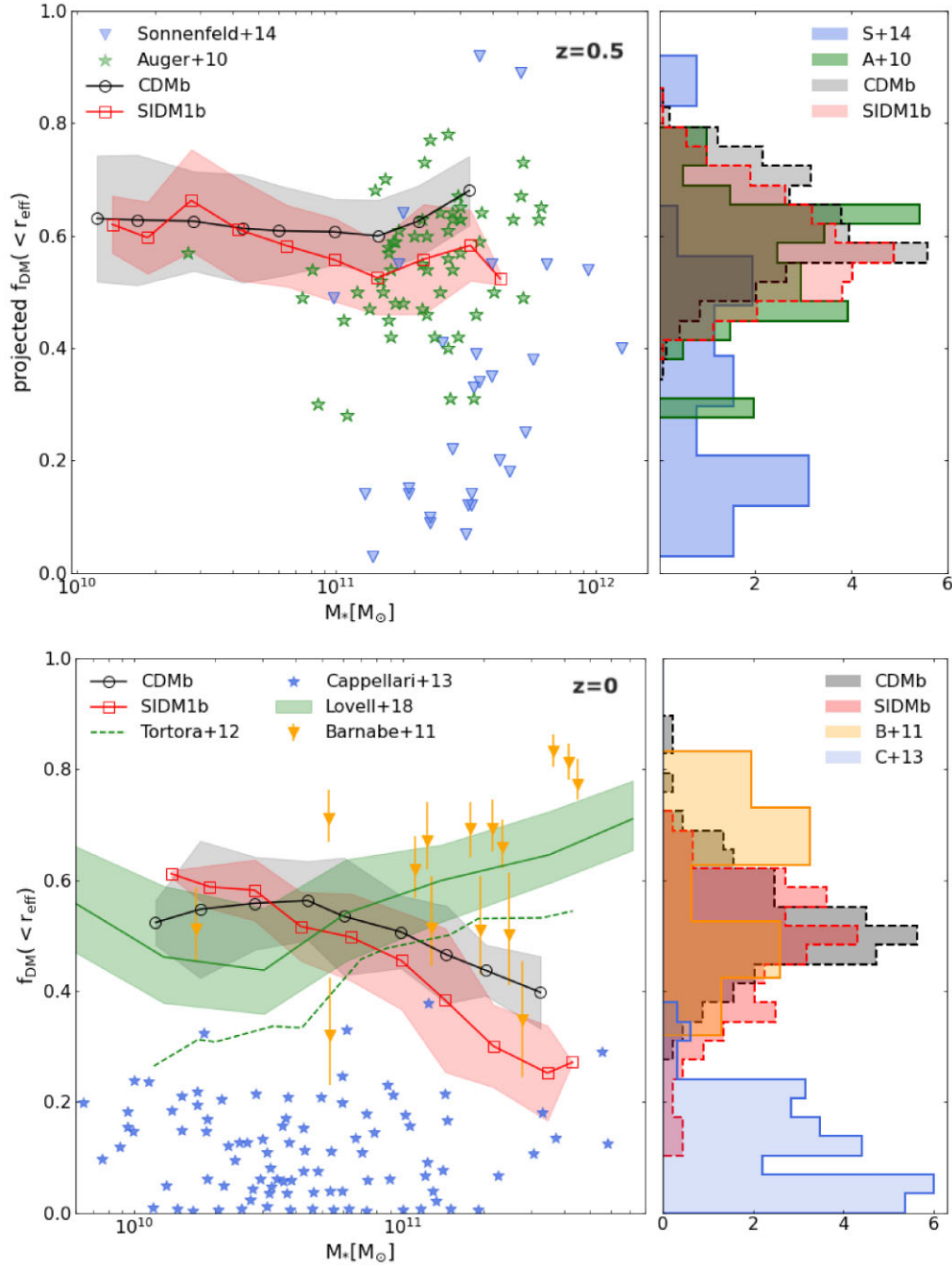


Figure 9. Comparison to observational results at $z = 0.5$ (top panels) and $z = 0$. (bottom panels). In the top-left panel, we show instead the *projected* DM fraction at $z = 0.5$, compared to values derived with gravitational lensing for the SLACS (Auger et al. 2010, green stars) and SL2S (Sonnenfeld et al. 2013, blue triangles) samples. For the simulated data we consider three different projections per halo. In the bottom-left panel, we plot the $z = 0$ 3D DM fraction f_{DM} within the effective radius r_{eff} , measured in the two hydro runs as a function of the galaxy stellar mass; the CDMb and SIDM1b distributions are represented by the black circles and red squares, respectively, together with their corresponding 1σ (shaded) region. We compare them with results from previous works based on simulations (Lovell et al. 2018, the TNG runs) or observations of Early-Type galaxies with: gravitational lensing (Barnabè et al. 2011, yellow triangles), dynamical (Jeans) modelling (Tortora et al. 2012, dashed line), and survey data (Cappellari et al. 2013, blue stars). In the smaller subpanels on the right, we compare the normalized distributions of simulated and observed fractions to each other.

It is worth pointing out that the SIDM1 DM-only run not only predicts smaller-separation lensed images, but quite often does not produce any strong lensing at all. In the left panel of Fig. 10, the total number of critical lines produced in SIDM1 is significantly lower than in the other three considered models (with a comparable total number of objects) and the configuration chosen in the right

panel does not produce any critical curves. These results are similar to the findings from Robertson et al. (2018a) on cluster scales and demonstrate that a large sample size is essential to obtain reliable predictions.

Finally, we compare the distribution of θ_E that we obtain from the hydro runs to observed values. In particular, we consider two

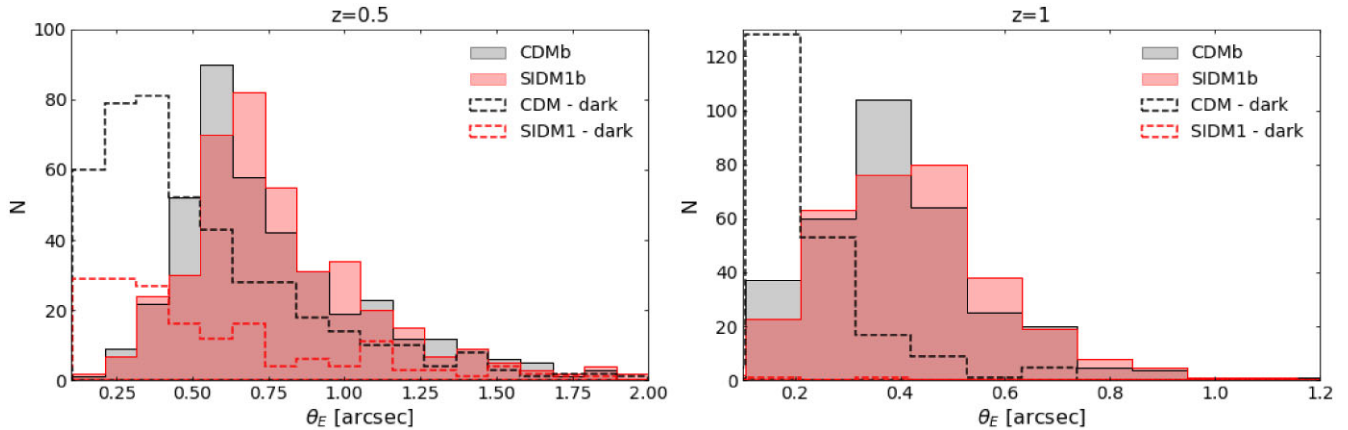


Figure 10. Sizes of the Einstein radii θ_E from the lensing convergence maps. We plot the distribution of the inferred sizes for the entire sample of haloes in the different runs. We consider three different projections per halo and two redshift configurations that corresponds to observed typical cases: lens systems at redshift $z_l = 0.5$ and sources at $z_s = 2.5$ (shown on the left panel) and lenses at redshift $z_l = 1$ with sources at $z_s = 3$ (on the right panel). The CDM and SIDM1 results are shown in black and red, respectively; empty dashed histograms stand for the results of the DM-only runs, while filled histograms show the hydro cases. At $z_l = 1$, the SIDM1 DM-only run produces critical curves only in a handful of cases and the θ_E distribution is thus barely visible in the plot.

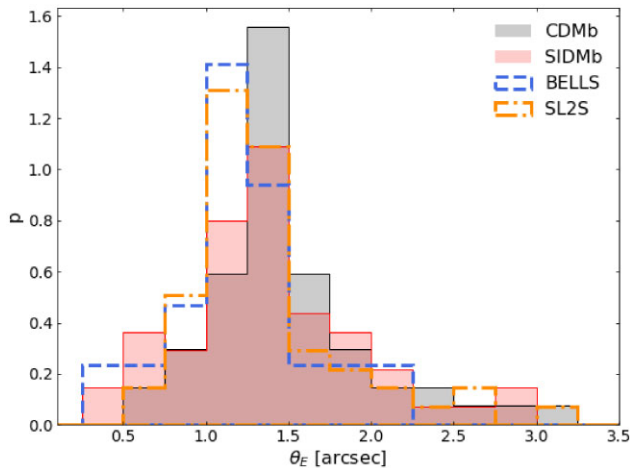


Figure 11. Comparison between the lensing properties of simulated haloes and real lens samples. Similarly to Fig. 10, the black and red filled histograms show the distribution of θ_E calculated from the CDMb and SIDM1b runs, respectively. However, here we use only the systems with a mass $M_{200} > 10^{13} M_\odot h^{-1}$ and we show only the results for $z = 0.5$ (with $z_s = 2.5$ as the source redshift), for a more precise comparison with two observational samples. These are the BELLS-Gallery (Ritondale et al. 2019) and SL2S (Sonnenfeld et al. 2013) lens samples, that include massive elliptical galaxies at $z_l \sim 0.5$ and $0.5 \leq z_l \leq 0.8$, with sources at $z_s \sim 2.5$. We compare the normalized distribution of Einstein radii derived in previous works to the sizes calculated from our simulations, finding a good agreement.

lens samples: the BELLS-Gallery (Ritondale et al. 2019) and SL2S (Sonnenfeld et al. 2013) lenses, that include massive elliptical galaxies at $z_l \sim 0.5$ and $0.5 \leq z_l \leq 0.8$, with sources at $z_s \sim 2.5$; previous works provide us with the inferred values of the Einstein radius for each system. We thus select haloes at $z = 0.5$ and with total masses $M_{200} > 10^{13} M_\odot h^{-1}$, corresponding to the mass range of ETGs. Fig. 11 shows the normalized distribution of θ_E for the two simulations and the two observed samples. We find a good agreement between the distributions, which is an encouraging indication of the fact that simulated systems are able to reproduce observed quantities. We point out again that, in this work, we do not explicitly select haloes on the basis of galaxy morphology, while observed lenses are

typically elliptical galaxies. However, the cut in halo mass allows us to select the most massive haloes, which most probably host massive ellipticals.

From Fig. 11, we conclude that we cannot distinguish between the cold and self-interacting DM hydro models by looking at the simulated sizes of the lensed images. This is somewhat in contrast with the results from Despali et al. (2019), who found a different distribution in the two models. While we cannot exclude that part of the difference is due to the different code and hydro model used for the simulations (Gadget with EAGLE model versus Arepo with TNG model), the main difference between the two is the size of the considered sample: Despali et al. (2019) used nine galaxies only, while here we have more than 100 systems per model and redshift. Moreover, the density profiles in Despali et al. (2019) showed a clear trend in SIDM with respect to CDM – that is, they were either cored or more cuspy than their CDM counterparts – while here we observe a larger range thanks to the improved statistics, more representative of the entire population.

6 CONCLUSIONS

SIDM has become an attractive alternative to CDM, due to its ability to produce a wider range of configurations that could solve the small-scale CDM problems, leaving the properties on large scale unchanged. However, these predictions have so far been based on DM-only simulations, while it is essential to understand how the interplay between self-interaction and baryonic effects can further modify the properties of haloes. For this purpose, we use the EAGLE cosmological simulations, that simulate the same volume of 50 Mpc^3 , in CDM and two SIDM models: one with constant cross-section ($\sigma/m = 1 \text{ cm}^2 \text{ g}^{-1}$) and one with a velocity-dependent cross-section. For each model, a DM-only and a full-hydrodynamic version are available, allowing us to study the effect of baryons and alternative DM models at the same time.

We select haloes in the mass range between $10^{12} \leq M_{200}/M_\odot h^{-1} \leq 10^{13.5}$ at $z = (0, 0.5, 1)$. We split our sample into mass bins in order to compare and average the features of haloes of comparable mass. To have a sufficient number of haloes for each bin, we divide our sample into 3 bins: $12.0 < \log(M_{200}/M_\odot h^{-1}) < 12.5$ (Low Mass), $12.5 < \log(M_{200}/M_\odot h^{-1}) < 13.0$ (Intermediate Mass), and $13.0 <$

$\log(M_{200}/M_{\odot} h^{-1}) < 13.5$ (High Mass) – given the volume of the simulations, we do not find higher masses.

We analyse the halo density profiles and concentrations, finding best fit parameters for the Einasto profiles and concentration–mass relation that describe our data. We proceed by measuring the DM fractions in the hydro runs and the predicted sizes of lensed images, if our haloes generated galaxy–galaxy lensing events. Further, we summarize our main results.

(i) In agreement with previous work, we find that in DM-only runs the spherically averaged density profiles of SIDM (SIDM1 and vdSIDM) haloes produce a central core with density lower by 50 per cent (or more) compared to the CDM case. We find that the inclusion of baryons reduces these differences between the density profiles in different DM models (to less than 20 per cent). Despite this, we find a weak trend with mass of the average final properties of SIDM density profiles in full-hydrodynamic runs: the most massive systems show cored profiles, while less massive ones have cusper profiles. This trend is related to the formation history of the halo, where the more massive haloes formed at lower redshift than the less massive ones and thus we see them at the stage in which the central core is established.

(ii) We fit the density profiles with the Einasto model and we repeat the fit twice, that is, leaving the shape parameter α_E free to vary or fixing it to $\alpha_E = 0.16$. We find that the profiles with fixed α_E well describe CDM haloes and all full-hydrodynamic runs, but fail to reproduce the central core for the DM-only SIDM runs (higher values are needed).

(iii) The concentrations of CDM and SIDM haloes, at fixed z , decrease monotonically with increasing halo mass. In the DM-only runs, we find that the $c - M$ relations have a similar slope in all models, but SIDM concentrations are lower than CDM ones: the core creation induced by self-interactions reduces the halo concentration similarly for all haloes. In the hydro runs, the SIDM relations are instead steeper than in CDM, due to the greater diversity of profiles and the dependence on mass found earlier. These differences translate into a small shift between the Einstein radius distributions: the least massive haloes in our sample are more concentrated in SIDM1b than in CDMb and thus produce a stronger lensing effect.

(iv) We calculate the DM fractions within the effective radius of the central galaxies r_{eff} and compare them to observational results. We find that at the high mass end, SIDM models can generate lower DM fractions. However, we do not predict values as low as some of the observations and thus the difference between the distributions of simulated and observed DM fractions has to be searched for elsewhere, that is, in biases between predicted and observed quantities or in more extreme alternative DM models. Methods able to distinguish between the DM and baryonic components in galaxies and clusters, performing a so-called ‘mass-decomposition’, constitute one of the most promising paths to discriminate between CDM and SIDM.

(v) We compare the distribution of Einstein radii that we obtain from the hydro runs to observed values. We find a good agreement between the distributions, which is an encouraging indication of the fact that simulated systems are able to reproduce observed quantities. However, we conclude that we cannot distinguish between the CDM and SIDM hydro models by looking at the simulated sizes of the lensed images.

In this work, we have analysed for the first time the properties of massive galaxies in a cosmological box that includes both self-interacting DM and baryons. In agreement with previous works, we find that the halo properties predicted in SIDM are deeply influenced by the inclusion of baryons. Recently, Eckert et al. (2022)

performed a similar analysis on the BAHAMAS-SIDM cluster-scale simulations (McCarthy et al. 2016; Robertson et al. 2018a). Through a comparison with the density profiles of observed galaxy clusters, they were able to put an upper limit on the self-interaction cross-section of $\sigma/m < 0.19 \text{ cm}^2 \text{ g}^{-1}$. Here, alternatively, we cannot exclude the higher value of $\sigma/m \sim 1 \text{ cm}^2 \text{ g}^{-1}$. In particular, we find that the SIDM models considered here cannot be ruled out at the scale of massive galaxies, contrary to previous claims. Eckert et al. (2022) also measured the Einasto shape parameter α_E at cluster scales and found that (in hydro simulations) it differs in different DM scenarios, and can be used to set constraints, while in our case the distribution of α_E is very similar for CDM and SIDM (see Fig. 3). This supports the hypothesis that a self-interacting model with a stronger velocity dependence could well explain the data on both scales, as recently suggested by other works (Correa 2021; Adhikari et al. 2022). It is fundamental to move forward in the field and investigate the interplay between baryons and alternative DM models, as it has successfully been done in the past for the CDM scenario.

ACKNOWLEDGEMENTS

This work used the DiRAC@Durham facility managed by the Institute for Computational Cosmology on behalf of the STFC DiRAC HPC Facility (www.dirac.ac.uk). The equipment was funded by BEIS capital funding via STFC capital grants ST/K00042X/1, ST/P002293/1, and ST/R002371/1, Durham University and STFC operations grant number ST/R000832/1. DiRAC is part of the National e-Infrastructure. LM and MM acknowledge the support from the grant number ASI n.2018-23-HH.0 and from the grant number PRIN-MIUR 2017 WSCC32. GD was supported by a Gliese fellowship at the University of Heidelberg. MM acknowledges support from PRIN Mainstream Projects 1.05.01.86.20 and 1.05.01.86.31, and the INFN InDark grant.

DATA AVAILABILITY

The catalogues and data products used for this paper can be made available upon reasonable request to the corresponding author.

REFERENCES

- Adhikari S. et al., 2022, preprint ([arXiv:2207.10638](https://arxiv.org/abs/2207.10638))
Aghanim N. et al., 2020, *A&A*, 641, 6
Arcadi G. et al., 2018, *Eur. Phys. J. C*, 78, 1
Auger M. W., Treu T., Bolton A. S., Gavazzi R., Koopmans L. V. E., Marshall P. J., Moustakas L. A., Burles S., 2010, *ApJ*, 724, L511
Barnabè M., Czoske O., Koopmans L. V. E., Treu T., Bolton A. S., 2011, *MNRAS*, 415, 2215
Bechtol K. et al., 2015, *ApJ*, 807, L50
Benitez-Llambay A., 2015, Py-Sphviewer: Py-Sphviewer V1.0.0, Zenodo
Bondarenko K., Sokolenko A., Boyarsky A., Robertson A., Harvey D., Revaz Y., 2021, *J. Cosmol. Astropart. Phys.*, 2021, 043
Boylan-Kolchin M., Bullock J. S., Kaplinghat M., 2011, *MNRAS*, 415, L40
Bullock J. S., Boylan-Kolchin M., 2017, *ARA&A*, 55, 343
Burkert A., 1995, *ApJ*, 447, L25
Cappellari M. et al., 2013, *MNRAS*, 432, 1862
Correa C. A., 2021, *MNRAS*, 503, 920
Davis M., Efstathiou G., Frenk C. S., White S. D., 1985, *ApJ*, 292, L371
Despali G., Sparre M., Vegetti S., Vogelsberger M., Zavala J., Marinacci F., 2019, *MNRAS*, 484, 4563
Despali G., Lovell M., Vegetti S., Crain R. A., Oppenheimer B. D., 2020, *MNRAS*, 491, 1295
Despali G., Walls L. G., Vegetti S., Sparre M., Vogelsberger M., Zavala J., 2022, *MNRAS*, 516, 4543

- Drlica-Wagner A. et al., 2015, *ApJ*, 813, L109
- Duffy A., Schaye J., Kay S., Dalla Vecchia C., 2008, *MNRAS*, 390, L64
- Dutton A. A., Maccio A. V., 2014, *MNRAS*, 441, 3359
- Eckert D., Ettori S., Robertson A., Massey R., Pointecouteau E., Harvey D., McCarthy I., 2022, *A&A*, 666, A41
- Einasto J., 1965, *Trudy Astrofizicheskogo Instituta Alma-Ata*, 5, 87
- Elbert O. D., Bullock J. S., Garrison-Kimmel S., Rocha M., Oñorbe J., Peter A. H., 2015, *MNRAS*, 453, 29
- Elbert O. D., Bullock J. S., Kaplinghat M., Garrison-Kimmel S., Graus A. S., Rocha M., 2018, *ApJ*, 853, L109
- Frenk C. S., White S. D. M., 2012, *Annalen der Physik*, 524, 507
- Fry A. B. et al., 2015, *MNRAS*, 452, 1468
- Gilman D., Birrer S., Nierenberg A., Treu T., Du X., Benson A., 2020, *MNRAS*, 491, 6077
- Hsueh J. W., Enzi W., Vegetti S., Auger M. W., Fassnacht C. D., Despali G., Koopmans L. V. E., McKean J. P., 2020, *MNRAS*, 492, 3047
- Kaplinghat M., Tulin S., Yu H.-B., 2014, *Phys. Rev. D*, 89, 035009
- Kaplinghat M., Valli M., Yu H.-B., 2019, *MNRAS*, 490, 231
- Kaplinghat M., Ren T., Yu H.-B., 2020, *J. Cosmol. Astropart. Phys.*, 2020, 027
- Klypin A., Kravtsov A. V., Valenzuela O., Prada F., 1999, *ApJ*, 522, 82
- Lovell M. R. et al., 2018, *MNRAS*, 481, 1950
- Lovell M. R., Zavala J., Vogelsberger M., 2019, *MNRAS*, 485, 5474
- McCarthy I. G., Schaye J., Bird S., Le Brun A. M. C., 2016, *MNRAS*, 465, 2936
- Meneghetti M., 2021, *Lecture Notes in Physics, Introduction to Gravitational Lensing*. Springer, Cham, p. 371
- Meneghetti M., Yoshida N., Bartelmann M., Moscardini L., Springel V., Tormen G., White S. D., 2001, *MNRAS*, 325, 435
- Meneghetti M. et al., 2020, *Science*, 369, 1347
- Meneghetti M. et al., 2022, *A&A*, 668, A188
- Miralda-Escudé J., 2002, *ApJ*, 564, L60
- Moore B., 1994, *Nature*, 370, 629
- Navarro J. F., Frenk C. S., White S. D. M., 1997, *ApJ*, 490, L493
- Oman K. A. et al., 2015, *MNRAS*, 452, 3650
- Peter A. H., Rocha M., Bullock J. S., Kaplinghat M., 2013a, *MNRAS*, 430, 105
- Peter A. H. G., Rocha M., Bullock J. S., Kaplinghat M., 2013b, *MNRAS*, 430, 105
- Planck Collaboration et al., 2014, *A&A*, 571, 16
- Ritondale E., Auger M. W., Vegetti S., McKean J. P., 2019, *MNRAS*, 482, 4744
- Robertson A., Massey R., Eke V., 2017, *MNRAS*, 465, 569
- Robertson A., Harvey D., Massey R., Eke V., McCarthy I. G., Jauzac M., Li B., Schaye J., 2018a, *MNRAS*, 488, 3646
- Robertson A. et al., 2018b, *MNRAS*, 476, L20
- Robertson A., Massey R., Eke V., Schaye J., Theuns T., 2021, *MNRAS*, 501, 4610
- Rocha M., Peter A. H. G., Bullock J. S., Kaplinghat M., Garrison-Kimmel S., Oñorbe J., Moustakas L. A., 2013, *MNRAS*, 430, 81
- Sameie O., Creasey P., Yu H.-B., Sales L. V., Vogelsberger M., Zavala J., 2018, *MNRAS*, 479, 359
- Sameie O., Yu H.-B., Sales L. V., Vogelsberger M., Zavala J., 2020, *Phys. Rev. Lett.*, 124, 141102
- Schaller M. et al., 2015, *MNRAS*, 452, 343
- Schaye J. et al., 2015, *MNRAS*, 446, 521
- Shen X., Brinckmann T., Rapetti D., Vogelsberger M., Mantz A., Zavala J., Allen S. W., 2022, *MNRAS*, 516, 1302
- Sonnenfeld A., Gavazzi R., Suyu S. H., Treu T., Marshall P. J., 2013, *ApJ*, 777, L97
- Spergel D. N., Steinhardt P. J., 2000, *Phys. Rev. Lett.*, 84, 3760
- Springel V., 2005, *MNRAS*, 364, 1105
- Springel V. et al., 2008, *MNRAS*, 391, 1685
- Tortora C., La Barbera F., Napolitano N. R., de Carvalho R. R., Romanowsky A. J., 2012, *MNRAS*, 425, 577
- Vogelsberger M., Zavala J., Loeb A., 2012, *MNRAS*, 423, 3740
- Vogelsberger M. et al., 2014, *MNRAS*, 444, 1518
- Vogelsberger M., Zavala J., Cyr-Racine F.-Y., Pfrommer C., Bringmann T., Sigurdson K., 2016, *MNRAS*, 460, 1399
- Vogelsberger M., Zavala J., Schutz K., Slatyer T. R., 2019, *MNRAS*, 484, 5437
- Yang D., Nadler E. O., Yu H.-B., 2023, *ApJ*, 949, L67
- Zavala J., Frenk C. S., 2019, *Galaxies*, 7, 81
- Zavala J., Vogelsberger M., Walker M. G., 2013, *MNRAS*, 431, L20

APPENDIX A: FITTING FORMULAE

In the standard CDM scenario, the DM haloes are well described by the NFW profile (Navarro et al. 1997), which, however, can fail to reproduce the cored profiles that characterize SIDM haloes. Here we test different alternative fitting formulae that have been used in the literature to describe the behaviour of SIDM haloes. Fig. A1 shows the mean SIDM1 density profiles for each mass bin and the different parametric best fits performed on these profiles, both for the hydro runs (top panels) and the DM-only runs (bottom panels).

We start with two-parameter formulae, namely the standard NFW profile (Navarro et al. 1997) and the Burkert profile (Burkert 1995):

$$\rho_B(r) = \frac{\rho_b r_b^3}{(r + r_b)(r^2 + r_b^2)}.$$

The Burkert profile, contrary to the NFW, is characterized by a core radius and it well describes the SIDM haloes in the DM-only runs (see bottom panels of Fig. A1), while it cannot reproduce the more cuspy behaviour in the hydro runs.

We then perform the fit using three-parameter formulae, namely the Einasto profile defined in Section 3 and a parametric profile proposed by Zavala et al. (2013):

$$\rho(r) = \frac{\rho_0 r_s^3}{(r + r_c)(r^2 + r_s^2)}, \quad (\text{A1})$$

which is similar to the Burkert profile but with two scale radii. Both profiles are able to well characterize the behaviour of SIDM haloes in both DM-only and hydro runs. Since the best fit parameter for each parametric profile have been found as the values that minimize the sum of the square residuals of $\log(\rho_{\text{model}}) - \log(\rho_i)$, to select which is the one that better describes our simulated haloes, we define the RMSD of the fit as

$$Q = \sqrt{\frac{1}{N_{\text{bin}} - 1 - p_{\text{free}}} \sum_i^{N_{\text{bin}}} (\log(\rho_{\text{model}}) - \log(\rho_i))^2}, \quad (\text{A2})$$

where N_{bin} is the number of bin used to perform the fit, p_{free} is the number of free parameters, ρ_{model} is the fitted density distribution, and ρ_i the mean density in each bin. Thus defined, Q gives an estimate of the goodness of the fit: the minimum Q would represent the best-fitting formula. Table A1 reports the values of Q for each formula both in DM-only and in hydro runs. For both hydro runs and DM-only runs we find that the Einasto profile has the minimum Q , with the only exception for the High mass bin in the DM-only simulation for which the Burkert and the Zavala+13 profiles have slightly lower Q values. Based on these results we decided to fit our haloes using the Einasto profile.

The last row of the Table also reports the Q values for an Einasto profile with fixed $\alpha_E = 0.16$, thus with only two free parameters: the results show that it represents a good fit for SIDM-hydro runs, but it does not work well in the DM-only case.

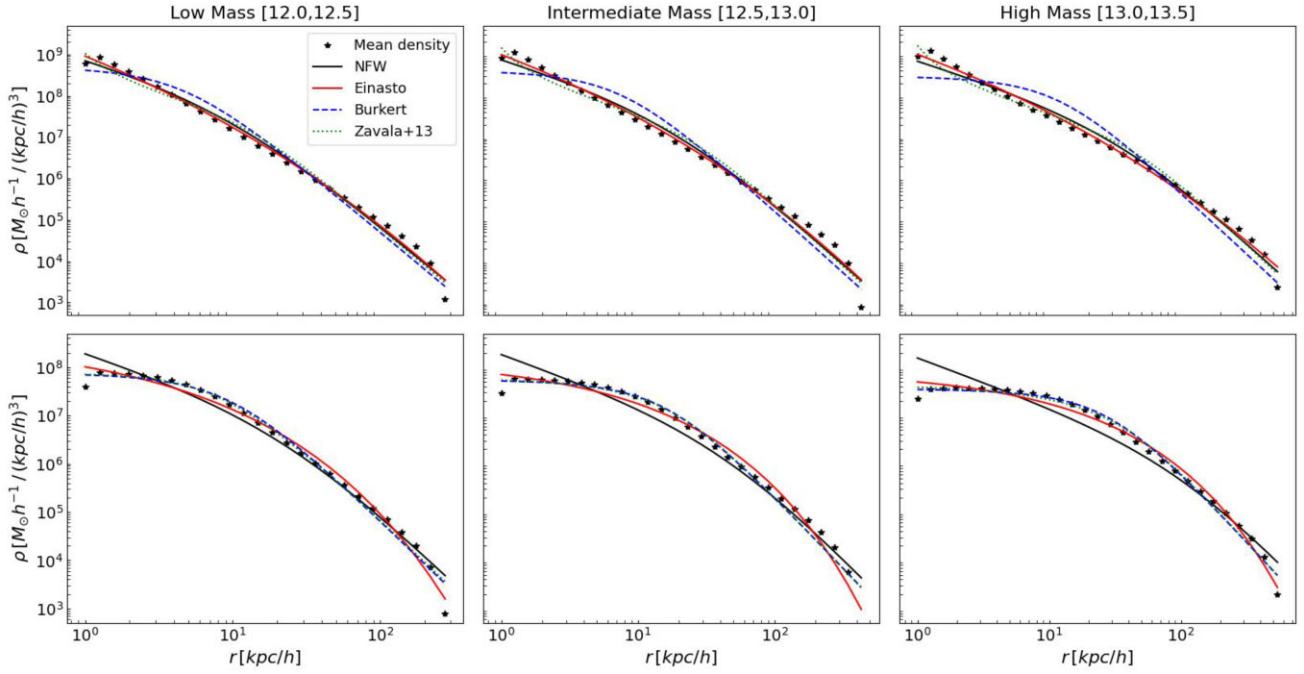


Figure A1. Different best-fitting relations fitted for the mean SIDM density profiles in the hydro-runs (top row) and DM-only runs (bottom row). Panels from left to right refer to Low Mass, Intermediate Mass, and High mass bins.

Table A1. The Q values as defined in the equation (A2), for each parametric profiles in both hydro and DM-only runs.

		Low mass	Intermediate mass	High mass
SIDM hydro runs	NFW	0.165	0.206	0.175
	Einasto	0.140	0.177	0.137
	Burkert	0.254	0.337	0.375
	Zavala+13	0.202	0.229	0.184
	Einasto($\alpha = 0.16$)	0.139	0.174	0.140
SIDM DM-only runs	NFW	0.253	0.333	0.316
	Einasto	0.162	0.188	0.135
	Burkert	0.172	0.222	0.126
	Zavala+13	0.173	0.226	0.128
	Einasto($\alpha = 0.16$)	0.292	0.374	0.339

This paper has been typeset from a $\text{\TeX}/\text{\LaTeX}$ file prepared by the author.